Wind Energ. Sci. Discuss., doi:10.5194/wes-2016-23, 2016
Manuscript under review for journal Wind Energ. Sci.
Published: 11 July 2016

Open Access
WIND ENERGY SCIENCE
DISCUSSIONS

Assessing Spacing Impact on the Wind Turbine Array Boundary Layer via Proper Orthogonal Decomposition

Naseem Ali, Nicholas Hamilton, and Raúl Bayoán Cal
Department of Mechanical and Materials Engineering,
Portland State University, Portland, OR 97207

Abstract

A 4 x 3 array of wind turbines was assembled in a wind tunnel with four cases to study the influence based on streamwise and spanwise spacings. Data are extracted using stereo particle-image velocimetry and analyzed statistically. The maximum mean velocity is displayed at the upstream of the turbine with the spacing of $6D$ and $3D$, in streamwise and spanwise direction, respectively. The region of interest downstream to the turbine confirms a notable influence of the streamwise spacing is shown when the spanwise spacing equals to $3D$. Thus the significant impact of the spanwise spacing is observed when the streamwise spacing equals to $3D$. Streamwise averaging is performed after shifting the upstream windows toward the downstream flow. The largest and smallest averaged Reynolds stress, and flux locates at cases $3D$ x $3D$ and $6D$ x $1.5D$, respectively. Snapshot proper orthogonal decomposition is employed to identify the flow coherence depending on the turbulent kinetic energy content. The case of spacing $6D$ x $1.5D$ possesses highest energy content in the first mode compared with other cases. The impact of the streamwise and spanwise spacings in power produce is quantified, where the maximum power is found in the spacing of $6D$ x $3D$.

PACS numbers:

Wind Energ. Sci. Discuss., doi:10.5194/wes-2016-23, 2016
Manuscript under review for journal Wind Energ. Sci.
Published: 11 July 2016

I. INTRODUCTION

Impacts on siting wind turbines in the wind farm include interaction between wakes, decreased wind velocity and an increased coalesce dynamic load on the downwind turbines. Turbine wakes lead to loss an average 10-20% of the total potential power output [1]. Extensive experimental and numerical studies focused on the wake properties in terms of mean flow characteristics and the specifications of the turbulent flow utilized to obtain optimal power production. Wake growth particularly depends on the shape and magnitude of the velocity deficit that relies on the ground roughness, flow above the canopy, and spacing between the turbines.

Chamorro and Porté-Agel [2] studied the influence of surface roughness on the wake as it alters the velocity distribution as well as turbulence levels. Cal *et al.* [3] noticed that the order of magnitude of kinetic energy entrainment is nearly equal to the power harvested by the wind turbine. Calaf *et al.* [4] used large Eddy simulation (LES) model to determine the roughness length scale of the fully developed wind turbine array boundary layer and quantified the impact of the correlation between the mean flow and turbulence. Meyers and Meneveau [5] compared aligned versus staggered wind farms; the latter yielding a 5% increase in extracted power. Chamorro and Porté-Agel [6] examined the wind farm under neutral stratification, observing flow can be divided into two regions that develop at different rates. The first region is located below the top tip and reaches the fully developed condition after the third row of turbines. The second region is located above the top tip where the flow modifies slowly. Hamilton *et al.* [7] investigated the effect of wind turbine configuration on the wake interaction and canopy layer. They considered standard Cartesian and row-offset configurations. The results showed that the maximum flux of kinetic energy increases about 7.5% in the exit row of offset configuration compared with the Cartesian arrangement. Hamilton *et al.* [8] studied the anisotropy of the Reynolds stress in the wake of wind turbine arrays in for counter-rotating turbines. The result showed that the greater magnitude of the flux can be entrained when the rotation direction of the blades is changed in a row-by-row configuration.

Although there are many studies dealing with the effect of the density of turbines on the wake recovery, it is still a debated question. The optimal spacing according to the Nysted farm is 10.5 diameters (D) downstream by 5.8D spanwise, whereas according to the Horns

Wind Energ. Sci. Discuss., doi:10.5194/wes-2016-23, 2016
Manuscript under review for journal Wind Energ. Sci.
Published: 11 July 2016

Rev farm is $7D$, optimal spacing along the bulk flow direction and $9.4D$ or $10.4D$ along the diagonal. Barthelmie and Jensen [9] showed that the spacing in the Nysted farm is responsible for 68-76% of the farm efficiency variation and for wind speed below 15 ms^{-1}, the efficiency will increase 1.3% for every one diameter increasing in spacing. Hansen *et al.* [10] pointed out that the variations in the power deficit for different spacing were almost negligible at approximately $10D$ into Horns Rev farm in spite of a large power deficit resulting from smaller turbine spacing. In addition, the mean power deficit is similar along single wind turbine rows when inflow direction is unified and the wind speed interval from 6 to 10 ms^{-1}. Furthermore, the maximum deficit happens between the first and the second row of turbines and minimum deficit in the remaining downstream. González-Longatt [11] found that when the downstream and spanwise spacing increased, the wake coefficient representing the total power output with wake effect over total power without wake effect increased, and the effect of the incoming flow direction on the wake coefficient increased when the spacing of the array is reduced. Meyers and Meneveau [12] studied the optimal spacing in fully developed wind farm with considerable limitations including neutral stratification and flat terrain with no topography. The results highlight that depending on the ratio of land cost and turbine cost, the optimal spacing might be $15D$ instead of $7D$. Stevens [13] used the effective roughness length performed by LES to predict the wind velocity at hub height depending on the streamwise and spanwise spacing, and the turbine loading factors. Also showing that optimal spacing depends on the wind farm length in addition to the factors suggested in [12]. Stevens *et al.* [14] used LES model to investigate the power output and wake effects in aligned and staggered wind farms with different streamwise and spanwise turbine spacing. In the staggered configuration, power output in fully developed flow depends mainly on the spanwise and streamwise spacings, whereas in the aligned configuration, power strongly depends on the streamwise spacing.

In this article, the proper orthogonal decomposition (POD) analysis will be employed to identify the structure of the turbulent wake associated with variation in spacing and understand the effect of the streamwise and spanwise on the characteristic flow of the wind turbine array, including Reynolds shear stress, turbulent flux and energy production.

Wind Energ. Sci. Discuss., doi:10.5194/wes-2016-23, 2016
Manuscript under review for journal Wind Energ. Sci.
Published: 11 July 2016

II. SNAPSHOT PROPER ORTHOGONAL DECOMPOSITION

Balancing between the gain and loss in energy can be quantified through the mean kinetic energy equation [15]. One of the main gain sources can be obtained by the spatial transport of energy by Reynolds shear stress, named the energy flux. The Reynolds shear stress is the center of the energy flux, therefore this study will focus on the energy flux to quantify the impact of the streamwise and spanwise spacing through the statistical analysis and using Proper orthogonal decomposition. POD is a mathematical tool that depends on a set of snapshots to obtain the optimal basis functions and decompose the flow into modes that express the most dominant features. This technique, which is presented in the frame of turbulence by Lumely [16], categorizes structures within the turbulent flow depending on their energy content and allows for filtering the structures associated with the low energy level. Sirovich [17] presented the snapshot POD that relaxes the difficulties of the classical orthogonal decomposition.

The flow field, taken as the fluctuating velocity, can be represented as $u_i = u(\vec{x}, t^n)$, where $\vec{x}$ and t^n refer to the spatial coordinates and time at sample n, respectively. A set of the orthonormal basis functions, ϕ, can be presented as

$$\phi_i = \sum_{n=1}^{N} A(t^n) u(\vec{x}, t^n). \tag{1}$$

The optimal functions have minimum averaged error and maximum averaged projection in mean square sense. The largest projection can be determined using the two point correlation tensor and Fredholm integral equation

$$\int_\Omega R(\vec{x}, \vec{x}^{'}) \phi(x^{'}) dx^{'} = \lambda \phi(x), \tag{2}$$

where $R(\vec{x}, \vec{x}^{'})$ is a spatial correlation between two points $\vec{x}$ and $\vec{x}^{'}$, N is the number of snapshots, T is the transpose of the matrix, and λ are the eigenvalues. The optimal deterministic problem is solved numerically as the eigenvalue problem. The eigenfunctions are orthogonal and have a corresponding positive and real eigenvalues organized by descending arrangement. The POD eigenvectors illustrate the spatial structure of the turbulent flow and the eigenvalues measure the energy associated with corresponding eigenvectors. The summation of the eigenvalues presents the total turbulent kinetic energy (E) in the flow domain. The fraction of the cumulative energy, η and the normalized energy content of each mode, ξ, can be represented as,

$$\eta_n = \frac{\sum_{n=1}^{n} \lambda_n}{\sum_{n=1}^{N} \lambda_n}, \tag{3}$$

$$\xi_n = \frac{\lambda_n}{\sum_{n=1}^{N} \lambda_n}. \tag{4}$$

POD tool is particularly useful in rebuilding the Reynolds shear stress using a set of eigenfunctions as follows,

$$\langle u_i u_j \rangle = \sum_{n=1}^{N} \lambda_n \phi_i^n \phi_j^n. \tag{5}$$

POD used to describe coherent structures of different types of flow such that axisymmetric mixing layer [18], channel flow [19], atmospheric boundary layer [20], wake behind disk [21], and subsonic jet [22]. In the frame of a wind turbine wake flow, Anderson *et al.* [23] applied POD to the flow in a wind farm simulated using LES. They showed the large scale motion and dynamic wake meandering are strongly governed by turbine spacing. The number of modes required to reconstruct the flow is related to the flow homogeneity. Hamilton *et al.* [24] investigated the wake interaction and recovery dynamic for Cartesian and row-offset wind array, showing that the flux of turbulence kinetic energy are reconstructed with approximately 1% of the total modes. Bastine *et al.* [25] performed analysis for a single wind turbine modeled *via* LES, observing the three modes is sufficient to capture the dynamic of the effective velocity over a potential disk. Recently, VerHulst and Meneveau [26] applied three dimensional POD on the LES data and quantified the contribution of each POD mode to the energy entrainment, finding that the net entrainment is relevant to the layout of the wind turbines in the field.

III. EXPERIMENTAL DESIGN

A 4 x 3 array of wind turbines was placed in the closed- circuit wind tunnel at Portland State University to study the effects due to variation in streamwise and spanwise spacing in a wind turbine array. The dimensions of the wind tunnel test section are 5 m (long), 1.2 m (wide) and 0.8 m (height). The entrance of the test section is conditioned by the passive

Wind Energ. Sci. Discuss., doi:10.5194/wes-2016-23, 2016
Manuscript under review for journal Wind Energ. Sci.
Published: 11 July 2016

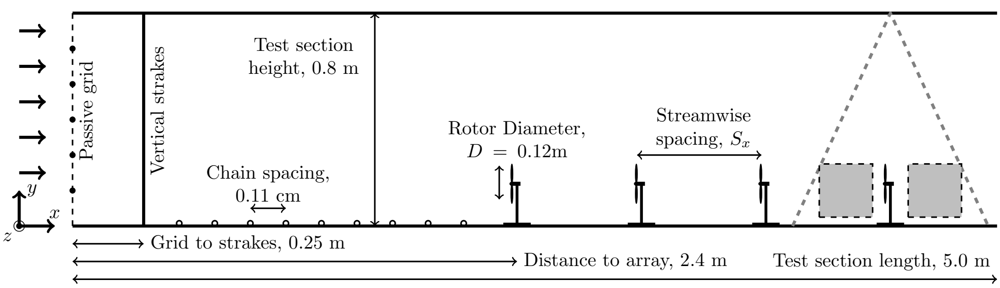

FIG. 1: Experimental Setup. Dashed gray lines indicate the placement of the laser sheet relative to the model wind turbine array. Filled gray boxes indicate measurement locations discussed below. Figure reproduced from Hamilton *et al.* [8].

grid, which consists of 7 horizontal and 6 vertical rods, to introduce large-scale turbulence. Nine vertical Plexiglas strakes located at 0.25 m downstream of the passive grid and 2.15 m upstream the first row of the wind turbine were used to modify the inflow. The thickness of the strakes is 0.0125 m with a spanwise spacing of 0.136 m. Surface roughness elements were placed on the wall as a series of chains with diameter of 0.0075 m and spaced 0.11 m apart. Figure 1 shows the schematic of experimental setup.

A 0.0005 m thick steel was used to construct 3 bladed wind turbine rotor. The diameter of the rotor was 0.12 m, equal to the height of the turbine tower. Each rotor blade was pitched at 15° out of plane at the root and 5° at the tip. These angles were chosen to provide angular velocity that correlates with required ranges of tip-speed ratio. A DC electrical motor of 0.0013 m diameter and 0.0312 m long formed the nacelle of the turbine and was aligned with flow direction. A torque sensing system was connected to the DC motor shaft following the design outlined in [27]. Torque sensor consists of a strain gauge, Wheatstone bridge and the Data Acquisition with measuring software to collect the data. For more information on the experiment conditions and data processing, see [7].

In this study, the flow field was sampled in four configurations of a model-scale wind turbine array, classified as Π_n, where n varies from 1 through 4 and considered in Table I. Permutations of streamwise spacing of $6D$ and $3D$, and spanwise spacing of $3D$ and $1.5D$ are examined. Stereoscopic particle image velocimetry (SPIV) was used to measure streamwise, wall-normal and spanwise instantaneous velocity at the upstream and downstream of the wind turbine at the center line of the fourth row as shown in figure 2. At each measurement

Wind Energ. Sci. Discuss., doi:10.5194/wes-2016-23, 2016
Manuscript under review for journal Wind Energ. Sci.
Published: 11 July 2016

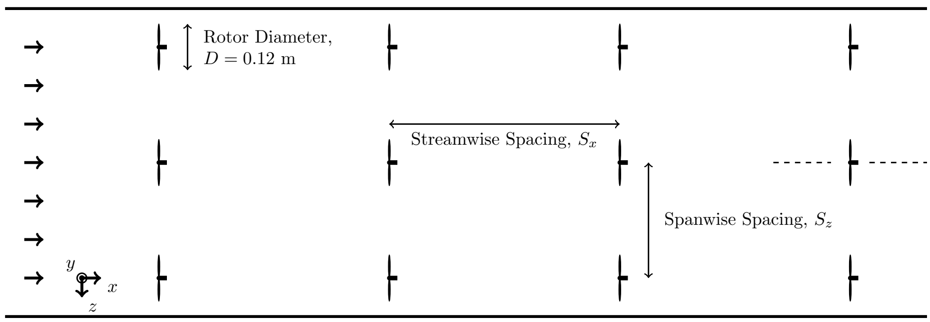

FIG. 2: Top view of 4 by 3 wind turbine array. The dash lines at the last row centerline turbine represent the measurement locations.

location, 2000 images were taken, to ensure convergence of second-order statistics. SPIV equipment is LaVision and consisted of an Nd:Yag (532nm, 1200mJ, 4ns duration) double-pulsed laser and four 4 MP ImagerProX CCD cameras positioned for the upstream and downstream of the wind turbine. Neutrally buoyant fluid particles of diethylhexyl sebecate were introduced to the flow and allowed to mix. Consistent seeding density was maintained in order to mitigate measurement errors. The laser sheet of 0.001 m thick with less than 5 mrad divergence angle is positioned and the measurement windows are 0.2 m x 0.2 m. A multi-pass Fast Fourier Transformation was used to process the raw data into vector fields. Erroneous measurement of the vector fields were replaced using Gaussian interpolation of neighboring vectors.

TABLE I: Streamwise and spanwise spacing of the experimental tests.

Cases	S_x	S_z	*Spacing Area*
Π_1	$6D$	$3D$	$18D^2$
Π_2	$3D$	$3D$	$9D^2$
Π_3	$3D$	$1.5D$	$4.5D^2$
Π_4	$6D$	$1.5D$	$9D^2$

IV. POWER MEASUREMENTS.

Figure 3 demonstrates the power produced, $\mathcal{F}_x$, that is obtained directly *via* the torque sensing system, versus the angular velocity, ω, for all cases. It is apparent from this figure

Wind Energ. Sci. Discuss., doi:10.5194/wes-2016-23, 2016
Manuscript under review for journal Wind Energ. Sci.
Published: 11 July 2016

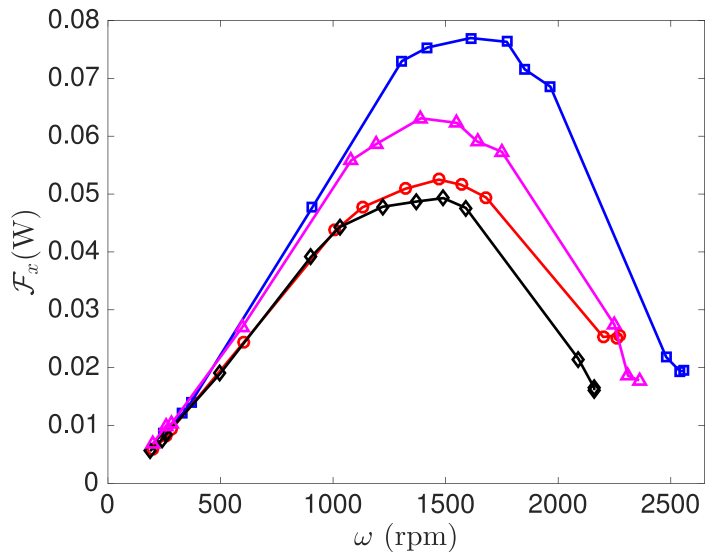

FIG. 3: Extracted power of the wind turbine at different angular velocities for four different cases Π_1 (□), Π_2 (◯), Π_3 (◊), and Π_4 (△).

that the maximum power are extracted approximately at angular velocity of 1500 ± 100 rpm. The optimal power of 0.078 W is harvested at the largest spacing, *i.e.*, case Π_1. Reducing streamwise spacing shows a significant decreasing in extracted power especially at $1000 < \omega < 1800$ rpm. The maximum power of case Π_2 is 33% less than case Π_1. The reduction ratio between cases Π_3 and Π_4 is 22%. Reducing spanwise spacing displays a majority at $x/D = 6$ where the reduction ratio of 20% is noticed. Small reduction ratio of 6% is identified between cases Π_2 and Π_3.

V. RESULTS

A. Statistical Analysis.

Herein, characterization of the wind turbine wake flow *via* mean velocity, Reynolds shear stress and kinetic energy, with the aim to understand the effect of turbine-to-turbine spacing. Figure 4 presents the streamwise velocity in upstream and downstream of the cases Π_1 through Π_4. The left and right contours of each case present the upstream and downstream flow, respectively. At upstream, case Π_1 attains the largest streamwise mean velocities

Wind Energ. Sci. Discuss., doi:10.5194/wes-2016-23, 2016
Manuscript under review for journal Wind Energ. Sci.
Published: 11 July 2016

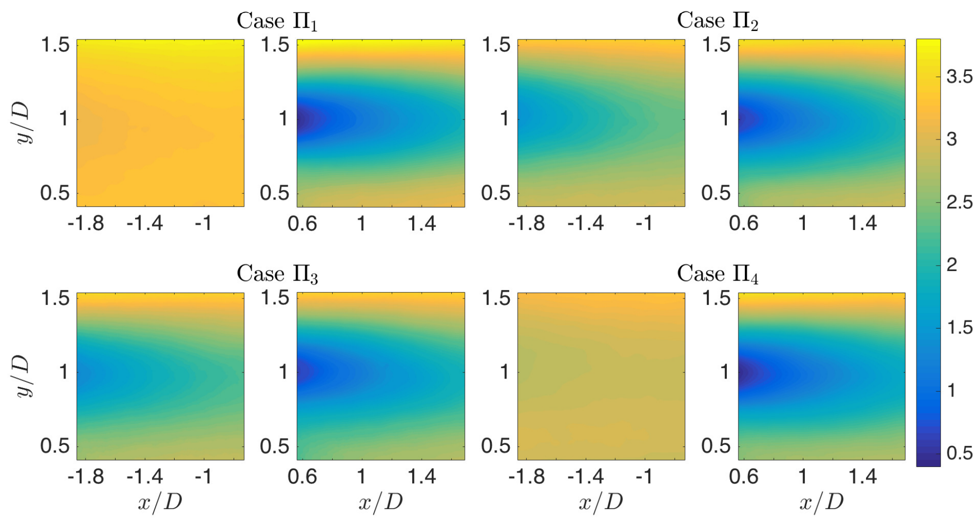

FIG. 4: Streamwise velocity at upstream and downstream of the cases Π_1 ($6D$ x $3D$), Π_2 ($3D$ x $3D$), Π_3 ($3D$ x $1.5D$), and Π_4 ($6D$ x $1.5D$).

compared with the other cases due to greater recovery of the flow upstream of the turbine. Although the streamwise spacing of case Π_4 is similar to case Π_1, the former shows reduced hub height velocity. The mean velocity is about 2.88 ms^{-1} compared with 3.3 ms^{-1} in case Π_1, confirming the influence of the spanwise spacing on wake evolution and flow recovery. Small variations are observed between case Π_2 and Π_3 above the top tip ($y/D = 1.5$) and below the bottom tip ($y/D = 0.5$), where case Π_2 demonstrates higher velocities. Downstream of the turbine, the four cases show clear differences especially above the top tip and below the bottom tip, where case Π_1, once again, shows the largest velocities. Case Π_2 also shows higher velocities below the bottom tip compared with cases Π_3 and Π_4. The comparison between case Π_3 and case Π_4 shows resemblance in velocity contour with exception at region $x/D < 0.8$, where case Π_4 displays the most significant velocity deficit.

Figure 5 contains the in-plane Reynolds shear stress $-\langle uv \rangle$ for the same cases as shown in figure 3. At upstream, cases Π_2 and Π_3 display higher stress compared with Π_1 and Π_4. Although the spanwise spacing of case Π_3 is half of case Π_2, no significant difference is apparent. The differences are quite revealing $0.5 \leq y/D \leq 1$, where case Π_2 exhibits heightened magnitudes of $-\langle uv \rangle$. At the downstream, comparison between the cases indicates that

Wind Energ. Sci. Discuss., doi:10.5194/wes-2016-23, 2016
Manuscript under review for journal Wind Energ. Sci.
Published: 11 July 2016

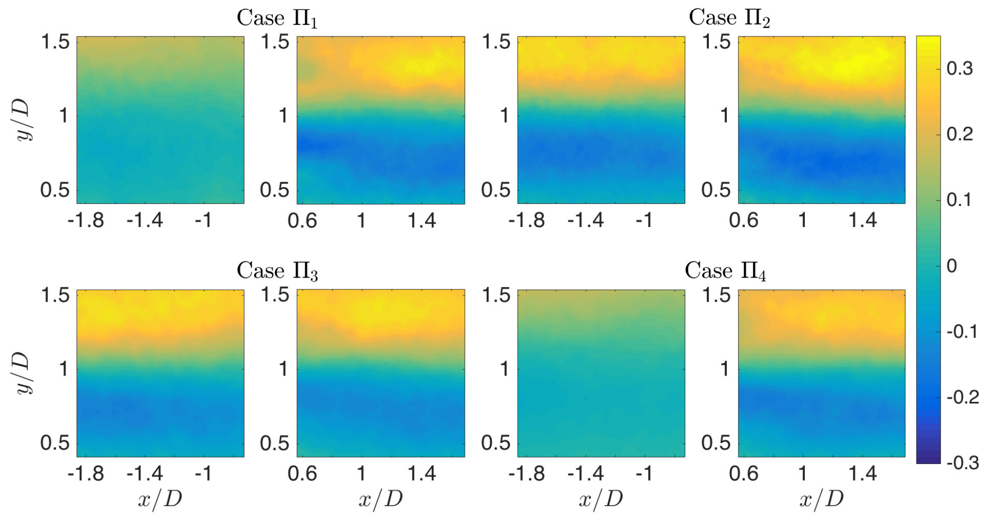

FIG. 5: Reynolds shear stress in upstream and downstream of the each measurement case.

reducing streamwise spacing increases the Reynolds shear stress. This difference is clearly observed comparing cases Π_2 and Π_1 at $x/D \geq 1$. The average over the downstream domain shows increasing of 16% in Reynolds shear stress of case Π_2. A similar effect is observed in case Π_3 where it exhibits higher stress than case Π_4 with increasing average of 2% is noticed. The spanwise spacing effect is more pronounced when the streamwise spacing is $3D$ as can be shown when comparing between case Π_3 and case Π_2 that shows increasing 20% in over domain average . However, decreasing spanwise spacing increases $-\langle uv \rangle$ slightly as shown when comparing between case Π_1 and Π_4. The difference of 6% is shown and the variation is observed only in a small region at ($y/D \approx 1.3$ and $x/D > 1.2$), where higher Reynolds shear stress is found in case Π_1.

Figure 6 displays the vertical flux of kinetic energy, $-\langle uv \rangle U$. At upstream, small variations are shown between case Π_1 and Π_4 mainly above the top tip as a result to higher mean velocity of case Π_1 at this location. The maximum $-\langle uv \rangle U$ is found at case Π_2 and Π_3. The variation between cases Π_2 and Π_3 shows that maximum negative flux is found at the regions between the hub height and bottom tip of case Π_2; higher positive flux is found above the top tip of the case Π_3. At downstream, case Π_1 displays the same energy flux distribution of case Π_4 with significant differences at the regions $x/D > 1.3$, where case Π_1

Wind Energ. Sci. Discuss., doi:10.5194/wes-2016-23, 2016
Manuscript under review for journal Wind Energ. Sci.
Published: 11 July 2016

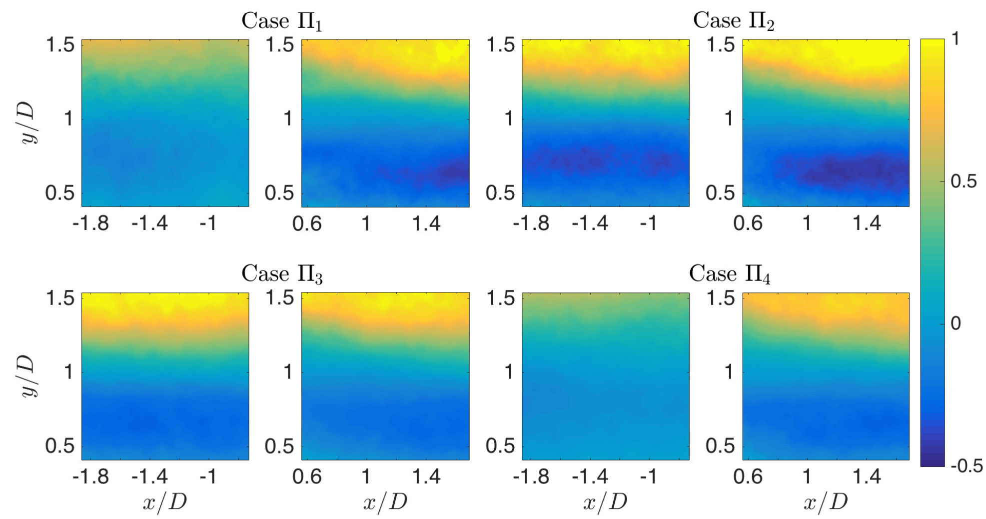

FIG. 6: Flux of kinetic energy in upstream and downstream of the each measurement case.

demonstrates higher energy flux. The average over downstream domain shows decreasing of 14% in $-\langle uv \rangle U$ of case Π_4. The same tendency is observed when comparing between cases Π_2 and Π_3 that shows decreasing about 24.5% in the the vertical flux. This result confirms that when the spanwise spacing decreases, the energy flux decreases also. Decreasing the streamwise spacing, case Π_2 exhibits higher $-\langle uv \rangle U$ than case Π_1 mainly when $x/D > 1$ and the increasing average is 15%. The similar behavior is observed when comparing between case Π_3 and Π_4. Case Π_3 displays higher $-\langle uv \rangle U$ of 5% than case Π_4 and the mainly differences are seen at $x/D > 1$ and $y/D \approx 1.5$. In general, the impact of streamwise spacing on energy flux is more pronounced when spacing $z = 3D$ than $1.5D$. The impact of spanwise spacing on energy flux is more pronounced when the spacing $x = 3D$ than $6D$. Also, case Π_2 shows higher $-\langle uv \rangle U$ comparing with other cases.

B. Averaged Profiles.

Spatial averaging of the variables is determined *via* shifting the upstream domain of each case beyond its respective downstream flow and performing streamwise averaging according to the procedure used in Cal *et al.* [3]. Spatial averaging makes it possible to compare

Wind Energ. Sci. Discuss., doi:10.5194/wes-2016-23, 2016
Manuscript under review for journal Wind Energ. Sci.
Published: 11 July 2016

the different cases while removing the streamwise dependence. Here, streamwise averaging is denoted by $\langle\cdot\rangle_x$. Figure 7(a) shows profiles of streamwise averaged mean velocity for all four cases. Case Π_1 and case Π_3 show the largest and smallest velocity deficits, respectively. At hub height, the velocity of case Π_1 is approximately 2.25 ms^{-1} whereas case Π_3 shows approximately velocity of 1.6 ms^{-1}. The difference between case Π_1 with case Π_4 is less than the difference between case Π_1 with case Π_2 confirming that the impact of reducing streamwise spacing is greater than changing the spanwise spacing. The influence of streamwise spacing is also observed when comparing cases Π_3 and Π_4. Interestingly, a reduction in streamwise spacing show less effect when the spanwise spacing $z/D = 1.5$. For example, the utmost disparity in streamwise velocity between the cases Π_1 and Π_2 is 0.57 ms^{-1} as opposed to the dissimilarity of 0.42 ms^{-1} between cases Π_3 and Π_4. Negligible variations are shown between the profile of cases Π_2 and Π_3. The cases Π_2, Π_3 and Π_4 converge at $y/D > 1.4$ while the case Π_2 and case Π_3 coalesce at the regions above the hub height. The trend of the averaged profiles of the streamwise velocity follows the same trend that is observed in the power curves, see figure 3, and that verify the relation between the power on the turbine with the deficit velocity.

Figure 7(b) contains the streamwise averaged Reynolds shear stress $-\langle uv\rangle$ for cases Π_1 through Π_4. Slight decreasing in $-\langle uv\rangle$ is attained in case Π_4 where the spanwise spacing is reduced. Reducing spanwise spacing shows an important influence when the streamwise spacing is $x/D = 3$. The noticeable discrepancies between case Π_2 and case Π_3 are found at the region below the hub height. Streamwise spacing differences play a more noteworthy role than variations in spanwise spacing. There are a significant variations between Reynolds shear stress of case Π_1 and case Π_2. The same trend holds when comparing between case Π_3 and Π_4. Interestingly, the largest difference between the Reynolds shear stress of cases is found between case Π_1 and case Π_2, located at $y/D \approx 0.7$ and $y/D \approx 1.4$. Furthermore, all four cases have approximately zero Reynolds shear stress at the inflection point located at hub height. In addition, the most striking result to emerge from averaged profiles is that case Π_2 displays the maximum Reynolds stress and case Π_4 presents the minimum stress.

Figure 7(c) presents streamwise average profile of the vertical flux of kinetic energy. Below the hub height, the difference cases Π_1 and Π_4 is small. The variation begins above the hub height and increases with increasing wall-normal distance due to the variation of the streamwise velocity of these two case as shown in figure 7(a). The significant variations

Wind Energ. Sci. Discuss., doi:10.5194/wes-2016-23, 2016
Manuscript under review for journal Wind Energ. Sci.
Published: 11 July 2016

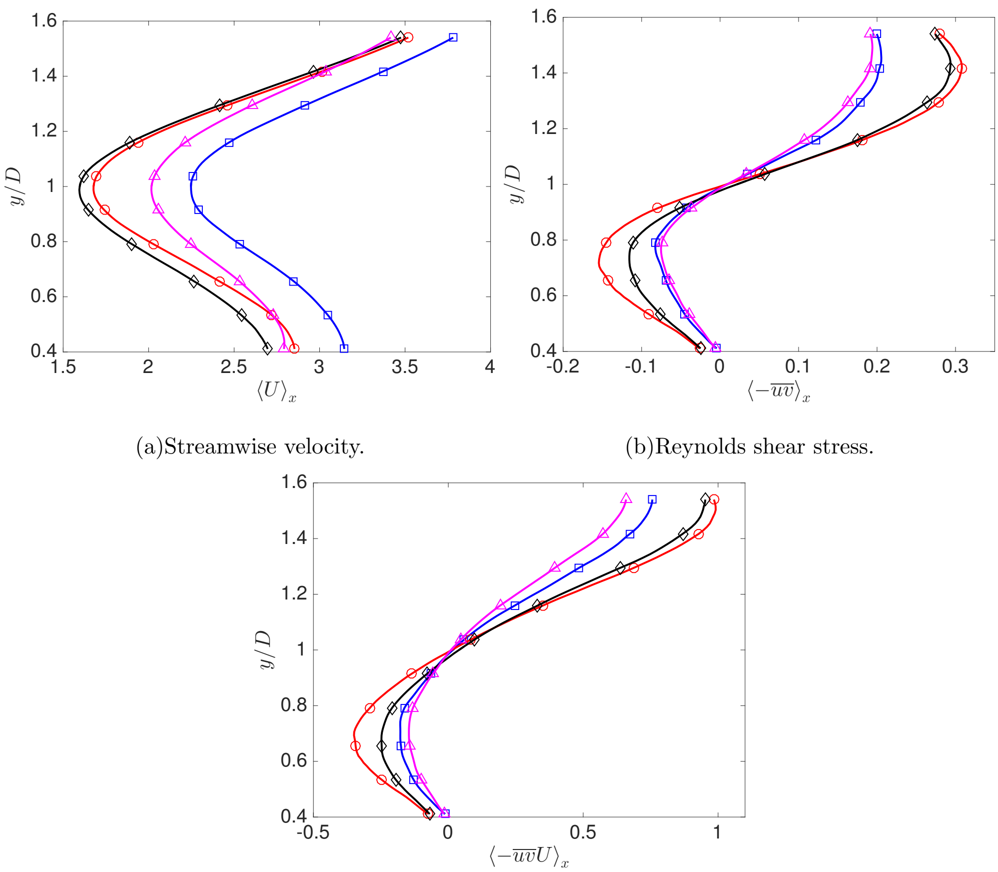

(a)Streamwise velocity.

(b)Reynolds shear stress.

(c)Energy flux

FIG. 7: Streamwise average profile of streamwise velocity, Reynolds shear stress, and energy flux and turbulent for four different cases Π_1 (□), Π_2 (○), Π_3 (◊), and Π_4 (△).

between case Π_2 and Π_3 are observed below the hub height due to the significant difference between the Reynolds shear stress of these two cases as can be shown in figure 7(b). Above the hub height, the difference between these cases is diminished. In general, when spanwise spacing decreases, the energy flux also decreases as shown when comparing between case Π_4 with case Π_2 and case Π_2 with case Π_3. In contrast, when streamwise spacing decreases, the energy flux increases as observed in comparing between case Π_1 with case Π_2 and case Π_3 with Π_4. The maximum and minimum flux are observed at case Π_2 and case Π_4, respectively. The region very close to the hub height also shows zero energy flux and changes the sign of the energy flux.

Wind Energ. Sci. Discuss., doi:10.5194/wes-2016-23, 2016
Manuscript under review for journal Wind Energ. Sci.
Published: 11 July 2016

C. Proper Orthogonal Decomposition.

Based on the POD analysis, the spatially integrated turbulent kinetic energy is expressed by the eigenvalue of each mode. Normalized cumulative energy, η_n, from Eq. (9) for upstream and downstream measurement windows are presented in the figure 8(a) and (b), respectively. Insets show the normalized energy content per mode, ξ_n, given by Eq. (10). At upstream flow, case Π_1 and case Π_4 converge faster than case Π_2 and Π_3, respectively. These results can be attributed to the reduction the streamwise spacing. Convergence of case Π_1 oscillates around the curve of case Π_4. The same trend is observed between case Π_2 and Π_3 but with fewer alternations. Modes 2 through 5 and modes 40 through 100 coincide in cases Π_1 and Π_4. Thus, convergence of case Π_2 is approximately coincident with case Π_3 except at mode 1 and modes 3 through 20. The inset of figure 8(a) indicates that the first mode of case Π_4 and case Π_3 contain higher energy content than the first mode of case Π_1 and case Π_2, respectively. The second mode of case Π_4 shows a greater decrease in energy content than case Π_1. Accounting for the convergence profile of cases Π_1 and case Π_4 at mode 2. The energy content, ξ_n, shows a trivial difference, $\mathcal{O}(10^{-3})$, between the four cases after mode 10. For the downstream flow, case Π_4 converges faster than the other cases, thereafter it is ordered as Π_1, Π_2 and Π_3 in succession. The oscillating behavior observed in the upstream flow, is noticed only between case Π_2 and Π_3. Beyond the tenth mode, the difference in energy content between four cases is lessened.

The comparison between the upstream and downstream reveals that energy accumulates in fewer modes in the upstream of each case, *e.g.*, case Π_1 requires 14 modes to obtain 50% of the total kinetic energy in upstream, whereas 26 modes are required to obtain the same percentage of energy downstream. A greater dissimilarity is observed between the convergence profile of case Π_1 and Π_4 at the downstream than the difference at the upstream. The contrast between case Π_1 and Π_4 is larger than the discrepancy between case Π_2 and Π_3 especially at downstream. The disparity between the upstream and downstream windows can be identified in the most energetic mode that shows the maximum and minimum variations at case Π_4 and case Π_3, respectively. This observation can be attributed to structure of the upstream flow of case Π_4 that is rather recovered, whereas the downstream show high deficit. However, the upstream and downstream of case Π_3 both show high velocity deficit, therefore the structure might be similar especially for large scale. For mode 2 through 10,

Wind Energ. Sci. Discuss., doi:10.5194/wes-2016-23, 2016
Manuscript under review for journal Wind Energ. Sci.
Published: 11 July 2016

eawe european academy of wind energy
Open Access WIND ENERGY SCIENCE DISCUSSIONS

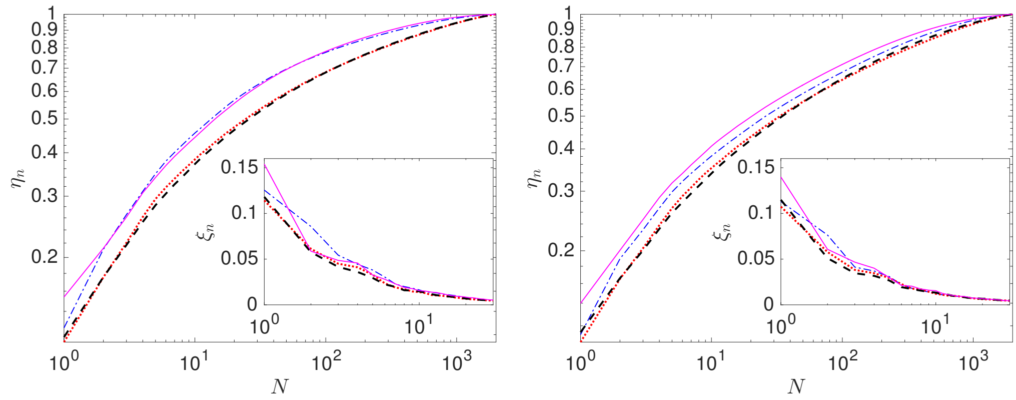

(a)Upstream. (b)Downstream.

FIG. 8: Energy content of the POD modes for four different cases: Π_1 ($- \cdot -$), Π_2 ($\cdots$), Π_3 ($--$), and Π_4 ($-$).

the biggest difference between the upstream and downstream is found in case Π_1.

Figure 9 presents the first modes at the upstream and downstream of the four different cases. The four cases show that small gradients in the streamwise direction compared with high gradient in the wall-normal direction. Although the four cases show divergence between the eigenvalues of the first mode, the eigenfunctions display rather analogous structures. The first POD mode shows variation of 1.25% when comparing between the upstream and downstream of case Π_1. Less important variations of 0.68% and 0.32% are observed in cases Π_2 and Π_3, respectively. Therefore, the structures of upstream and downstream of these cases are approximately equivalent. Upstream of case Π_3 looks like the opposite of its downstream. Similarity is observed between case Π_1 and Π_4 although the energy difference between them about 3%. Case Π_4 presents significant differences between the upstream and downstream mainly at $y/D \approx 1.5$ and the region between the hub height and bottom tip.

Figure 10 presents the fifth mode at the upstream and downstream of the four cases that show a mixture of POD and Fourier (homogenous) modes in the streamwise direction. Although the fifth mode of the four cases contain $\approx$ 74% less energy of than the first mode, large scales are still pronounced. Small scales also appeared in the upstream and the downstream windows of the four cases. Upstream windows of cases Π_1, Π_2, and Π_3 show the opposite structure of its own downstream windows. Interestingly, the upstream and downstream widows of case Π_3 look like the reduced scale of the it own first mode. The

Wind Energ. Sci. Discuss., doi:10.5194/wes-2016-23, 2016
Manuscript under review for journal Wind Energ. Sci.
Published: 11 July 2016

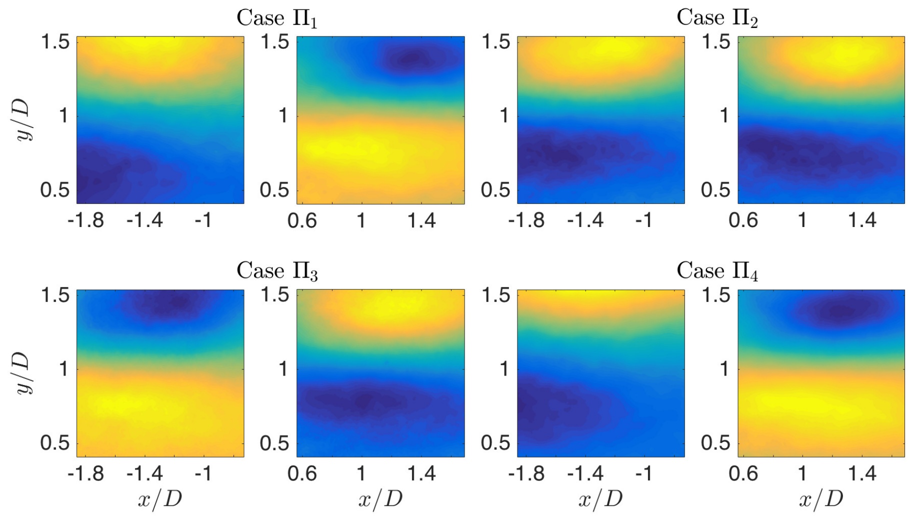

FIG. 9: The first mode at upstream and downstream of the each case.

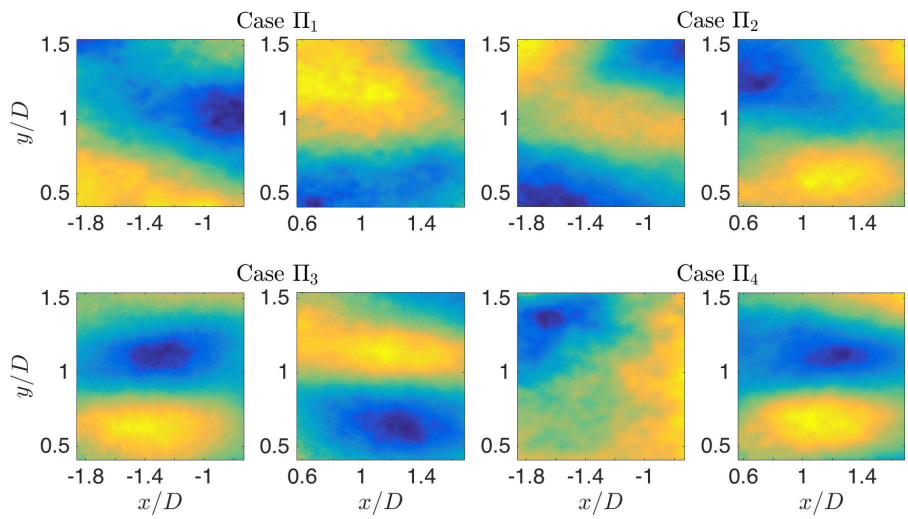

FIG. 10: The fifth mode at upstream and downstream of the each case.

303 same trend is observed in the downstream window of case Π_4.

304 Figure 11 presents the twentieth mode at the upstream and downstream of the four
305 cases. Small structures become noticeable in both upstream and downstream windows.
306 The upstream of cases Π_1 and Π_4 show large scale structure compared with the other two

Wind Energ. Sci. Discuss., doi:10.5194/wes-2016-23, 2016
Manuscript under review for journal Wind Energ. Sci.
Published: 11 July 2016

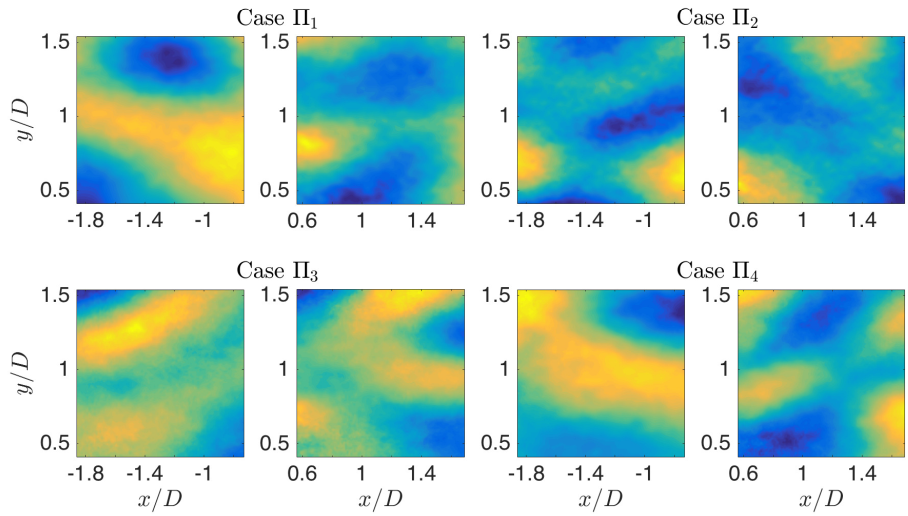

FIG. 11: The twentieth mode at upstream and downstream of the each case.

cases. Although, after mode 10, there is no significant energy content difference between the cases as shown in figure 7, the structure of the modes show significant discrepancy. This observation somewhat surprising and will confirm that the intermediate modes show the association with the inflow characterizations.

D. Reconstruction Averaged Profile.

Streamwise averaged profiles of Reynolds shear stress are reconstructed according to Eq. (12). Partial amounts of the turbulent kinetic energy are considered using a few modes to reconstruct the stress. In this study, first mode, first 5, 10, 25, and 50 modes are used to reconstruct the stress as shown in figure 12. The inset of figure present the Reynolds shear stress construction using the modes 5-10, 5-25, and 5-50, respectively. The black lines are the streamwise average of full data from figure 7(b). Using an equal number of modes, case Π_4 rebuilds the profiles of the Reynolds shear stress faster than the other cases. Case Π_1 also show fast reconstruction of profiles. Dissimilarity with case Π_4 is mainly in the profile of first mode (red line) and the first five modes (blue line). Cases Π_2 and Π_3 show approximately the same trends in reconstruction profiles. Below hub height, the four cases show the same trend of the first mode profiles where there is a zero contribution to the reconstruction profiles.

Wind Energ. Sci. Discuss., doi:10.5194/wes-2016-23, 2016
Manuscript under review for journal Wind Energ. Sci.
Published: 11 July 2016

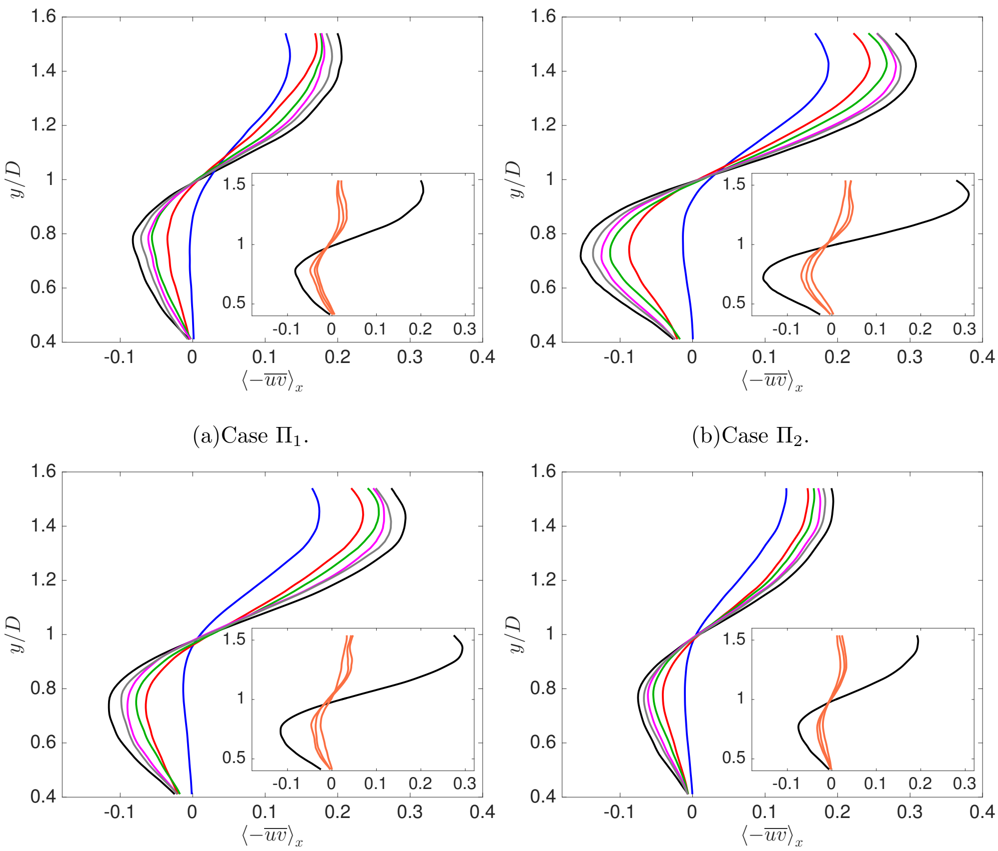

(a)Case Π_1.

(b)Case Π_2.

(c)Case Π_3.

(d)Case Π_4.

FIG. 12: Reconstruction Reynolds shear stress using: first mode (—), first 5 modes (—), first 10 modes (—), first 25 modes (—) and first 50 modes (—). Full data statistics (—). The insets show the reconstruction using modes 5-10, 5-25, and 5-50 (—).

The first five modes display exactly the form of the full data profile in each case. Maximum difference between the successive reconstruction profiles displays between the first mode and first five profiles. Cases Π_1 and Π_2 show a moderate variation between the first five and first ten (green line) profiles. After the first ten profiles, the contribution in reconstruction is small as shown magenta and gray lines. Using more successive modes leads to more accurate reconstruction. Generally, the maximum difference between the full data profiles and the reconstructed profiles is located at $y/D \approx 0.75$ and $y/D \approx 1.4$ where the extrema in $\langle \overline{uv} \rangle_x$ are located.

To quantify the contribution of the small scale structures, Reynolds shear stress is recon-

Wind Energ. Sci. Discuss., doi:10.5194/wes-2016-23, 2016
Manuscript under review for journal Wind Energ. Sci.
Published: 11 July 2016

structured using the intermediate modes. As can be shown in the insets of figure 12, the full data profile (black line) is compared with profiles reconstructed from modes 5-10, 5-25, and 5-50 (peach lines). Surprisingly, the intermediate modes in each case approximately take the form of the full data profiles below the hub height. Reconstruction Reynolds shear stress in Case Π_1 and Π_4 show minute variations between the successive reconstruction profiles and approximately take form of vertical lines above the hub hight. This trend is opposite to the trend that is shown in the first mode profile. Cases Π_2 and Π_3 show a difference between the successive profiles above the hub height. The maximum difference is observed between the reconstructed profiles from modes 5-10 and from 5-25.

VI. CONCLUSIONS

Stereographic PIV data are used to assess characteristic quantities of the flow field in a wind turbine array with varied streamwise and spanwise spacing. The flow fields are analyzed and compared statistically and *via* snapshot proper orthogonal decomposition. Streamwise velocity, Reynolds shear stress, and vertical energy flux are presented in upstream and downstream of the considered cases. In the inflow measurement window, higher velocities are observed in cases Π_1 and Π_4 comparing with the other two cases whose inflows are unrecovered wakes from leading rows. In contrast, case Π_2 and Π_3 show higher Reynolds shear stress, and energy flux. Downstream fields show the higher influence of streamwise spacing when the spanwise spacing of $z = 3D$. Thus, the significant effect of the spanwise spacing is observed when the streamwise spacing of $x = 3D$. To remove the streamwise dependence, streamwise average profiles of the statistical quantities are computed. Averaged profiles of the velocity follow the order of higher velocity seen in the contour plots in case Π_1 and lowest velocity in case Π_3. The maximum and minimum difference are observed between cases Π_1 with case Π_3 and Π_2 with case Π_3. Averaged profile of Reynolds shear stress, and energy flux show the same sequence where the maximum and minimum locate in case Π_2 and case Π_4, respectively.

Based on the POD analysis, the upstream of the four cases converges faster than the downstream flow. The fastest convergence is associated with case Π_1 and Π_4 in upstream, and with case Π_4 in the downstream. Higher energy associated with first mode is observed in case Π_4 in both upstream and downstream flow. No significant difference in energy con-

Wind Energ. Sci. Discuss., doi:10.5194/wes-2016-23, 2016
Manuscript under review for journal Wind Energ. Sci.
Published: 11 July 2016

tent after the mode 10 between the for cases. Streamwise averaged profiles of the Reynolds shear stress are reconstructed using the back projecting coefficient and the set of eigenfunctions. Higher energetic mode and small energetic modes are used individually to show the contribution depends on the four cases. Case Π_4 rebuild the averaging profile faster than other cases. Same trend in reconstruction is observed in cases Π_2 and Π_3. The small scale structure is responsible to take the shape of the profiles exactly.

Power produced is measure directly using torque sensing system. The power curves exactly follow the trend of the velocity profiles. The maximum power extracted at angular velocity of 1500 ± 100 and it is harvested in case Π_1. Small difference in harvested power is observed between cases Π_2 and Π_3. The findings of this study have a number of the practical implications especially in the tight wind farm when the large areas are not available. A continue efforts are required to understand the impact of streamwise and spanwise spacing in infinity array flow with different stratification conditions.

Acknowledgments

The authors are grateful to NSF-ECCS-1032647 for funding this research.

---

[1] R. J. Barthelmie, S. T. Frandsen, M. Nielsen, S. Pryor, P.-E. Rethore, and H. Jørgensen, Wind Energy **10**, 517 (2007).

[2] L. P. Chamorro and F. Porté-Agel, Boundary-layer meteorology **132**, 129 (2009).

[3] R. B. Cal, J. Lebrón, L. Castillo, H. S. Kang, and C. Meneveau, Journal of Renewable and Sustainable Energy **2**, 013106 (2010).

[4] M. Calaf, C. Meneveau, and J. Meyers, Physics of Fluids **22**, 015110 (2010).

[5] J. Meyers and C. Meneveau, AIAA **827**, 2010 (2010).

[6] L. P. Chamorro and F. Porté-Agel, Energies **4**, 1916 (2011).

[7] N. Hamilton, M. Melius, and R. B. Cal, Wind Energy **18**, 277 (2015).

[8] N. Hamilton and R. B. Cal, Physics of Fluids **27**, 015102 (2015).

[9] R. J. Barthelmie and L. Jensen, Wind Energy **13**, 573 (2010).

[10] K. S. Hansen, R. J. Barthelmie, L. E. Jensen, and A. Sommer, Wind Energy **15**, 183 (2012).

Wind Energ. Sci. Discuss., doi:10.5194/wes-2016-23, 2016
Manuscript under review for journal Wind Energ. Sci.
Published: 11 July 2016

[11] F. González-Longatt, P. Wall, and V. Terzija, Renewable Energy **39**, 329 (2012).

[12] J. Meyers and C. Meneveau, Wind Energy **15**, 305 (2012).

[13] R. J. Stevens, Wind Energy p. 10.1002/we.1857 (2015).

[14] R. J. Stevens, D. F. Gayme, and C. Meneveau, Wind Energy **19**, 359 (2016).

[15] T. Cebeci, *Analysis of Turbulent Flows with Computer Programs* (Butterworth-Heinemann, 2013).

[16] J. L. Lumley, Atmospheric Turbulence and Radio Wave Propagation pp. 166–178 (1967).

[17] L. Sirovich, Quarterly of Applied Mathematics **45**, 561 (1987).

[18] M. N. Glauser and W. K. George, in *Advances in Turbulence* (Springer, 1987), pp. 357–366.

[19] P. Moin and R. D. Moser, Journal of Fluid Mechanics **200**, 471 (1989).

[20] S. Shah and E. Bou-Zeid, Boundary-Layer Meteorology **153**, 355 (2014).

[21] M. Tutkun, P. V. Johansson, and W. K. George, AIAA **46**, 1118 (2008).

[22] S. Tirunagari, V. Vuorinen, O. Kaario, and M. Larmi, CSI Journal of Computing **1**, 20 (2012).

[23] S. J. Andersen, J. N. Sørensen, and R. Mikkelsen, Journal of Turbulence **14**, 1 (2013).

[24] N. Hamilton, M. Tutkun, and R. B. Cal, Wind Energy **18**, 297 (2015).

[25] D. Bastine, B. Witha, M. Wächter, and J. Peinke, Journal of Physics: Conference Series **524**, 012153 (2014).

[26] C. VerHulst and C. Meneveau, Physics of Fluids **26**, 025113 (2014).

[27] H. S. Kang and C. Meneveau, Measurement Science and Technology **21**, 105206 (2010).